www.elsevier.com/locate/memsci

Facile fabrication of poly(ε-caprolactone)/graphene oxide membranes for bioreactors in tissue engineering

Nazely Diban, Sandra Sanchez-González, Maria Lázaro-Díez, Jose Ramos-Vivas, Ane Urtiaga

PII: S0376-7388(17)30692-0
DOI: http://dx.doi.org/10.1016/j.memsci.2017.06.052
Reference: MEMSCI15364

To appear in: *Journal of Membrane Science*

Received date: 13 March 2017
Revised date: 5 June 2017
Accepted date: 20 June 2017

Cite this article as: Nazely Diban, Sandra Sanchez-González, Maria Lázaro-Díez Jose Ramos-Vivas and Ane Urtiaga, Facile fabrication of poly(ε caprolactone)/graphene oxide membranes for bioreactors in tissue engineering *Journal of Membrane Science,* http://dx.doi.org/10.1016/j.memsci.2017.06.052

Facile fabrication of poly(ε-caprolactone)/graphene oxide membranes for bioreactors in tissue engineering

Nazely Diban[a*], Sandra Sanchez-González[a], Maria Lázaro-Díez[b,c], Jose Ramos-Vivas[b,c], Ane Urtiaga[a]

[a]Department of Chemical and Biomolecular Engineering, ETSIIyT, University of Cantabria, Avda. Los Castros s/n, 39005 Santander, Spain

[b]Servicio de Microbiología, Hospital Universitario Marqués de Valdecilla e Instituto IDIVAL, Santander, Spain

[c]Red Española de Investigación en Patología Infecciosa (REIPI), Instituto de Salud Carlos III, Madrid, Spain

[*]Corresponding Author: *Department of Chemical and Biomolecular Engineering. University of Cantabria. Av. de los Castros s/n. 39005 Santander, Spain. E-mail: dibann@unican.es*

Abstract

Promising polymer membranes of blended biocompatible poly(ε-caprolactone) and graphene oxide (PCL/GO) and PCL and partially reduced graphene oxide (PCL/rGO) with outstanding water and nutrient transport properties for cell culture bioreactors were prepared using phase inversion at mild temperatures. Some of the prepared PCL/GO membranes were subjected to a 'chemical-free' GO post-reductive process using UV (PCL/GO/UV) irradiation. The PCL/rGO membranes exhibited 2.5 times higher flux than previously reported biocompatible polymer membranes for cell culture bioreactors, which was attributed to the highly interconnected porosity. On the other hand, the formation of PCL-graphene oxide composites in the PCL/GO and PCL/GO/UV membranes was not conclusive according to spectroscopic analyses, thermal analyses and mechanical characterization, probably due to the low graphene oxide loading in the membranes (0.1%w/w). The presence of graphene oxide-based nanomaterials in the polymer matrix slightly reduced the mechanical properties of the PCL-graphene oxide membranes by limiting the polymer chain mobility in comparison to that of the plain

PCL membranes. However, their mechanical stability was sufficient for the applications pursued. Finally, the biocompatibility assay indicated that the incorporation of GO and rGO into the PCL matrix enhanced the uniform distribution and morphology of the glioblastoma cells on the surface of the PCL-graphene oxide membranes.

Keywords: Graphene oxide-based nanomaterials; Perfusion bioreactors; Phase inversion; Poly(ε-caprolactone) membranes; Tissue engineering

1. INTRODUCTION

The medical field represents one of the most relevant markets for membranes when compared to other industrial applications, aside from the water industry [1]. Different relevant applications for membranes in medicine include drug delivery, haemodialysis, artificial organs and tissue engineering. Membranes for tissue engineering can be used as scaffolds for cells to be implanted in vivo to enhance cell differentiation in tissues and in bioreactors for in vitro cell culture proliferation and regeneration of in vitro 3D tissues. The 3D tissues regenerated by this technology can be further implanted in vivo or used as alternatives to animal models for drug screening or artificial organ supports. Particularly, perfusion bioreactors, using membranes as scaffolds, provide a series of benefits, such as reducing the internal and external diffusive limitations for nutrient transport. Furthermore, perfusion bioreactors enable the application of mechanical stimuli on cultured cells, in contrast to other bioreactor designs for tissue engineering [1,2].

The phase inversion casting technique is a versatile and facile method for producing highly porous scaffolds with nanofibrous structures and scalable, 3D, commercial membrane products. Phase inversion is the most important method employed for

developing nanocomposite polymer membranes for water treatment applications [3]. For example, antifouling nanocomposite polyethersulfone (PES) membranes for ultrafiltration and nanofiltration have been produced by dispersing carbon nanotubes [4], TiO_2 particles [4] or graphene oxide (GO) [5] in the polymer solution prior to phase inversion. Similarly, to fabricate scaffolds for tissue engineering, the incorporation of nanomaterials, such as carbon nanotubes (CNT) [6], graphene [7], hydroxyapatite (HA) [8,9], and silver nanoparticles [10,11], in different polymer matrices to achieve mechanical reinforcement or to favour chemical or electrical cell stimuli or antibacterial properties has been investigated [12].

Due to the outstanding structural, optical, mechanical, thermal and electrical properties of graphene and its derivatives, these materials have been used in different application niches, such as energy, electronics, and biomedicine [13, 14]. Particularly, the electroactivity of neural cells has promoted the use of graphene and its derivatives for neural tissue regeneration [15]. The biocompatibility and toxicity of graphene and graphene derivatives has been the source of controversial discussion among the research community. The thorough revision by Volkov et al. [16] showed the potential cytotoxicity of graphene and graphene derivatives and the potential risks under different types of exposures to these nanomaterials. However, they also found multitude of other interesting experimental works, where graphene and graphene derivatives demonstrated their improved biocompatibility for different biomedical applications, included implantable devices and regenerative medicine. Meanwhile long-term cytotoxic effects of graphene and its derivatives are elucidated, the potentiality of these nanomaterials should be explored. In our previous work [17], poly(ε-caprolactone) (PCL) membranes fabricated using phase inversion exhibited high porosity and a morphology that enhanced the adherence and proliferation of the neural type cells. We consider that the

incorporation of small amounts of graphene oxide-based nanomaterials in our former PCL membranes may improve the intrinsic properties of the polymer matrix [18], i.e., mechanical reinforcement, electrical and/or thermal conductivity, nutrient flux and antifouling as well as ameliorating the intrinsic PCL-neural cell biocompatibility. The most common fabrication method used to produce PCL/GO composite scaffolds for tissue engineering is electrospinning [19-21]. In addition, electrospun composites of PCL with commercial graphene [22] and graphene produced using arc discharge methods [23] have been prepared. Ramzani and Karimi [24] compared the loading effects of graphene nanomaterials on the mechanical properties of electrospun composites of PCL with GO and rGO, respectively, and observed a critical graphene loading of 0.1wt% in the PCL. While novel needleless electrospinning techniques have recently improved the production of electrospun fibers at large scale (up to 1.6 m) [25, 26], the technique still does not reach the production scale (hundreds of meters) that can be achieved by means of phase inversion. Alternative methods to electrospinning for producing PCL/GO nanocomposites that have been reported in the literature involve solvent casting methods using complex and extreme temperature conditions and chemicals [21, 27] or laborious and time consuming in situ polymerization techniques [28]. However, to our knowledge, the formation of PCL-graphene oxide composite membranes to be used as scaffolds in bioreactors for tissue engineering using the simple phase inversion technique under mild conditions has not been reported previously in the literature.

In this work, flat membranes of GO or partially reduced graphene oxide (rGO) with PCL were produced using phase inversion under mild temperature conditions and in the absence of toxic reductive chemicals. The effects of the oxidation state of the graphene oxide nanomaterials on the morphological, chemical and thermal characteristics and

mechanical and nutrient transport properties of the PCL-graphene oxide membranes were assessed. The possible formation of PCL-graphene oxide nanomaterial composites was evaluated. Additionally, glioblastoma cell culture tests were conducted as preliminary tests for the biocompatibility of the membranes prepared in this study for use in bioreactors for neural tissue engineering.

2. EXPERIMENTAL

2.1 Materials

PCL pellets (Mw, 80 kDa), bovine serum albumin (BSA, A9647, Fraction V, p≥ 96%) and dibasic sodium phosphate (Na_2HPO_4) were supplied by Sigma Aldrich, (Spain). Graphite powder (99%) and N-methyl pyrrolidone (NMP, 99%, extrapure) were purchased from Acros Organics. Sulfuric acid (95-98%) (H_2SO_4), hydrochloric acid (37%) (HCl), potassium permanganate ($KMnO_4$), sodium nitrate ($NaNO_3$), sodium chloride (NaCl), potassium chloride (KCl) and potassium dihydrogen phosphate (KH_2PO_4) were provided by Panreac. Hydrogen peroxide (H_2O_2, 30% v/v) was purchased from Scharlab (Spain), and 2-propanol (IPA, 99%) was obtained from Oppac (Spain). The aliphatic solvent, Shellshol D70, was supplied by Shell Chemicals (The Netherlands). All reagents were used as purchased.

2.2 Synthesis of the graphene oxide and reduced graphene oxide

GO was synthesized by chemical oxidation of graphite powder following a modified Hummer's method [29, 30]. Briefly, 3 g of graphite powder and 1.5 g of $NaNO_3$ were added to 70 mL of H_2SO_4, and the mixture was stirred in an ice bath. Next, 9 g of $KMnO_4$ was slowly added to the solution at a constant temperature of 35˚C over 20 minutes. Afterwards, ultrapure water was added, and the temperature was raised to 98˚C for 15 minutes. The excess of $KMnO_4$ was removed with H_2O_2 and washed with

ultrapure water to obtain graphite oxide. The graphite oxide was exfoliated using ultrasonication (VCX 500, Sonics & Materials, Inc., USA) for 30 minutes and centrifuged (Centrifuge 5810, Eppendorf, Spain) for 1 h. The GO powder was dried at 50˚C for 24 h.

Reduced graphene oxide (rGO) was synthesized using a hydrothermal method with the GO produced previously, according to an adapted method from Ribao et al. [30]. In summary, the GO was redispersed in ultrapure water (0.5 mg/mL) by sonication and heated at 200˚C during 3 h in a Teflon lined autoclave. The rGO precipitated during this process. The rGO was finally dried at 50˚C for 24 h.

2.3 Preparation of the PCL-graphene oxide flat membranes

The casting and phase inversion techniques described elsewhere for plain PCL scaffolds [17] were adapted here for preparing the PCL-graphene oxide flat membranes. First, a dispersion of GO or rGO in NMP was prepared using sonication for 30 minutes. After that, PCL was added in the GO/NMP or rGO/NMP dispersion and stirred (Roller Shaker 6 Basic, IKA, Spain) for 48 h at 37°C until achieving a uniform PCL solution. The weight percentages of PCL and the GO (PCL/GO) or rGO (PCL/rGO) nanomaterials in the polymer solution were 15%w/w and 0.1%w/w, respectively. The nanomaterial loading was selected based on the critical loading of 0.1wt% that was found by Ramzani and Karimi [24] during the preparation of PCL-graphene composites using electrospinning techniques. In addition, it was experimentally observed that using a 1%w/w graphene loading led to mechanically unstable membranes (see Figure S1 of Appendix A. Supplementary material). Lower loading concentrations (0.25 and 0.5%w/w) were also tested unsuccessfully. The polymer solution was left to degasify overnight at room temperature and casted on a glass plate using a doctor blade casting knife through a 0.2 mm slit. The casted solution was immediately submerged into a

100%v/v IPA coagulation bath until the polymer film was completely precipitated. Then, the membrane was placed into a new IPA coagulation bath to complete the solvent exchange for 24 h. To completely remove the solvent traces, the PCL/GO and PCL/rGO films were subsequently immersed in ultrapure water that was changed periodically during 72 h. Furthermore, certain PCL/GO membranes were subjected to a UV post-treatment using a UV lamp (365 nm, 6 W, Model EA-160/FE, Spectroline, USA) for 48 h, for the purpose of reducing the graphene oxide present in the PCL/GO membrane. The membranes obtained from this procedure are referred to as PCL/GO/UV. Control membranes containing only PCL (15%w/w PCL in NMP) were also prepared for comparison.

2.3 Physical characterization

The structure and morphology of the surface and cross section of the PCL-graphene oxide membranes were determined using scanning electron microscopy (SEM, EVO MA 15, Carl Zeiss, Germany) at a voltage of 20 kV. For the cross-section images, the samples were frozen in liquid nitrogen and fractured. All the samples were kept overnight at 30˚C under vacuum and were gold sputtered before examination.

The thickness of the flat scaffolds, δ, was measured using an electronic micrometer (Standard, Series 293, Mitutoyo, Spain), and the overall porosity, ε, was quantified using a gravimetric method, similar to that of Diban et al. [17]. Samples of the membranes were prepared and allowed to dry in a vacuum oven at 30°C for 24 h. The samples were then weighed (W_2) (AT21 Comparator, Mettler Toledo, Spain) and subsequently submerged in Shellshol D70 for 24 h. The excess solvent was wiped with a tissue paper, and the samples were weighed again (W_1). The value of ε was calculated according to the following equation:

$$\varepsilon\,(\%) = \frac{(W_1 - W_2)/\rho_{Solv}}{(W_1 - W_2)/\rho_{Solv} + W_2/\rho_{PCL}} \times 100 \qquad (1)$$

where ρ_{Solv} is the density of Shellshol D70 (0.8 g/cm^3 at 25°C) and ρ_{PCL} is the density of PCL (1.145 g/cm^3 at 25°C) [31]. The measurements were done in triplicate. Additionally, surface porosity of the films, ε_s, was estimated from the surface SEM images using ImageJ software (ImageJ 1.51 d (2016), Wayne Rasband National Institutes of Health, USA).

The quality of the synthesized GO and rGO and the presence of GO or rGO in the PCL-graphene oxide membranes were characterized using Fourier transform infrared (FTIR) spectroscopy (Spectrum 65 spectrometer, Perkin Elmer, Spain) with an ATR sampling accessory (GladiATR, PIKE Technologies, USA).

Thermal gravimetric analyses (TGA) were carried out on a DTG-60H thermobalance (Shimadzu, Germany) with a scanning range from room temperature up to 650°C and a heating rate of 10˚C min^{-1} under a nitrogen atmosphere. The mass of the film samples ranged from 5 to 10 mg. Differential scanning calorimetry (DSC) with the PCL-graphene oxide membranes were conducted using DSC-131 instrumentation (SETARAM Instrumentation, Germany). The samples (5-10 mg) were heated from room temperature to 100˚C at a rate of 10˚C min^{-1}. After a stabilization period of 10 minutes at 100°C, the sample was cooled down to 0˚C at 10°C min^{-1}, stabilized for 10 minutes and finally heated again to 100°C at the same rate. The degree of crystallinity, χ_C (%), was determined using equation (2) [28]:

$$\chi_C = \frac{\Delta H_m}{(1-\beta)\Delta H_m^0} \qquad (2)$$

where β is the mass fraction of GO or rGO in the PCL film, ΔH_m is the sample melting enthalpy from the second heating ramp and ΔH_m^0 is the melting enthalpy for a 100%

crystalline PCL (139.5 J g^{-1} [28]).

Axial tensile tests of the films were conducted using specimens of 40×6 mm^2 mounted on a servo-hydraulic testing universal machine (SERVOSIS, ME-400, Spain) with a load cell capacity of 1.25 kN at a constant speed of 8 mm/s, according to the ISO standard for thin plastic films (ASTM D882- 12). The average values of the tensile properties were obtained from two replicates.

2.4 Membrane flux characterization

The hydraulic and nutrient permeability were determined using a homemade cross-flow filtration setup (Figure 1) that consisted of a film holder with a 10 cm^2 effective filtration area, A_e. The polymer membrane divided the holder cell into a feed and permeate compartment. The feed was contained in a 2 L feed reservoir with an electrical heating coil (Selecta, Spain) to warm the feed solution to a temperature of 37°C. A peristaltic pump (model 323E, Watson Marlow, Germany) drove the feed liquid at a flow rate of 90 mL min^{-1} through the feed compartment of the membrane test cell, and it was recirculated back to the feed reservoir. A valve located at the exit of the cell was used to maintain the feed chamber at a pressure slightly above atmospheric pressure. The permeate side was opened to the atmosphere. The permeate stream was continuously collected, and its weight was automatically recorded in real time.

The hydraulic permeability of the membranes was determined as follows: the feed reservoir was filled with ultrapure water (18.2 MΩ cm, Milli-Q water, Millipore, Spain) and heated to 37˚C. Then, the water pressure through the film was maintained at 0.20 bar for 1 h for film preconditioning and flux stabilization. Afterwards, the flux was measured at fixed pressure values during up-down pressure cycles within 0.05 to 0.20 bars for each membrane specimen. The water flux, $J_w (Lm^{-2}h^{-1})$, at each pressure was calculated using equation (3), where A_e (m^2) is the effective membrane surface area and

Δt (h) is the time period of permeate collection. The hydraulic permeance, P_w ($Lm^{-2}h^{-1}bar^{-1}$), was calculated using the slope of the water flux vs. pressure (ΔP) plot according to equation (4).

$$J_w = \frac{W_{w,permeated} \times \rho_{w,37°C}}{\Delta t \times A_e} \quad (3)$$

$$P_w = \frac{J_w}{\Delta P} \quad (4)$$

For determining the nutrient permeance, a synthetic solution of the model protein, BSA (0.4 g L^{-1}), in a phosphate buffer solution (PBS, pH 7.4) was prepared. The films were preconditioned in a similar manner as the hydraulic permeance flushing ultrapure water at 0.1 bar for 1 h. Then, the BSA solution was circulated at 37 °C through the feed side of the membrane test cell at 0.1 bar, and the permeate liquid was collected for 4 h. The total BSA solution flux, J_T ($L\ m^{-2}h^{-1}$), and total BSA solution permeance, P_T ($L\ m^{-2}h^{-1}bar^{-1}$), were calculated in a similar manner as the water permeation experiments. The BSA rejection ($R_{BSA,}$ %) was calculated according to equation (5). The BSA concentration in the feed and permeate streams ($C_{BSA}^{f}\left(mg\ L^{-1}\right)$ and $C_{BSA}^{p}\left(mg\ L^{-1}\right)$, respectively) were measured using UV spectrometry (UV-1800 Shimadzu) at a fixed wavelength of 280 nm.

$$R_{BSA} = \left(1 - \frac{C_{BSA}^{p}}{C_{BSA}^{f}}\right) \times 100 \quad (5)$$

Both the hydraulic and nutrient permeation tests were conducted in duplicate for each membrane. The data are presented as the mean values ± average deviation.

2.5 Biocompatibility tests and static cell cultures

The U87 human glioblastoma cell line (ATCC® HTB-14™) was maintained in Dulbecco's-modified Eagle's medium (DMEM, Gibco Invitrogen, USA) supplemented

with 10% calf serum and antibiotic agents (penicillin G (100 U mL^{-1}) and streptomycin (100 mg mL^{-1})) in a humidified atmosphere of 5% carbon dioxide and 95% air at 37°C. The scaffolds were placed on flat-bottom 6-well plates (Corning, Inc., USA) and sterilized by immersion in a 70% ethanol solution for 5 minutes.

The cells were trypsinized from culture flasks, resuspended in culture medium, and seeded uniformly onto the membranes at a cell density of 1×10^4 cells mL^{-1}. Plates containing the membranes and cells were kept in a humidified atmosphere of 5% carbon dioxide and 95% air at 37°C and incubated for different periods of time: 1 day, 6 days and 14 days.

After incubation, the cells were fixed in cold paraformaldehyde (3% in PBS) for 20 minutes at room temperature, permeabilized with Triton X-100 (0.1% in PBS) for 5 minutes at room temperature, and washed three times with PBS. Fluorescent-labelled phalloidin (Atto-590, Sigma Aldrich, Spain), which interacted with the polymerized f-actin, was used to identify the actin filaments and fibres. During microscopy observation, the membranes were inverted, and a series of optical sections were obtained with a Nikon A1R confocal scanning laser microscope (Nikon Corporation, Japan) using a Plan Apo VC 20X DIC N2 objective and equipped with a 561 nm laser. Reconstructions of the confocal sections were assembled using NIS Elements 3.2 software.

3. RESULTS AND DISCUSSION

3.1. Physical characterization

According to the characterization of TiO_2-graphene oxide nanocomposites that were prepared previously in our group [30] using similar exfoliation and hydrothermal reduction protocols, the GO and rGO prepared herein were expected to form

nanoplatelets that were 1-4 graphitic films thick. Micro-photographs of the GO and rGO nanomaterials (Figure S2 of Appendix A. Supplementary Material) show evidences of delamination into few layers. The surface in rGO nanomaterial seems to be more uniform than in GO and therefore in rGO nanomaterials there was a homogeneous distribution of the number of layers, while in GO particles different number of layers seemed to be overlapped. The dynamic light scattering (DLS) characterization results of the particle size distributions of GO and rGO dispersed in NMP are shown in Figure S3 (Appendix A. Supplementary Material) and indicate that the average particle sizes of the dispersed GO and rGO were 295 and 825 nm, respectively. These results might indicate the agglomeration of the rGO particles dispersed in NMP. Similar shapes and size particle distributions for GO and rGO nanomaterials (823 and 529 nm, respectively) measured by DLS were reported by Kumar et al. [7]. However, in that study, the chemical reduction of GO led to a reduction in the average particle size. Additionally, a small fraction of GO and rGO particles with average sizes of 4801 and 5560 nm, respectively, was observed. Because the graphene oxide particles were not spherical, the particle sizes determined from the spherical approximation model of the DLS technique may not have been accurate. Anyways, DLS might preferentially measure the length/width of the nanoparticles instead of their thickness. Besides, the TEM images of the TiO_2-graphene oxide nanomaterial previously described by Ribao et al. [30] demonstrated the nanoplatelet shapes of the nanomaterials prepared similarly as the GO and rGO reported herein.

Cross-section and surface SEM images showing the morphology of the membranes are shown in Figure 2. The values of the membrane thickness and porosity (bulk and surface) are reported in Table 1. The membranes presented porous sponge-like structures that are characteristic of phase-separated polymer membranes. The

thicknesses of the membranes containing GO and rGO nanoplatelets did not significantly change in comparison to the plain PCL membranes. All the PCL-graphene oxide membranes presented a highly interconnected porosity throughout their thickness. The PCL, PCL/GO and PCL/GO/UV membranes presented a homogeneous porosity that was similar to that of previously reported PCL membranes [17, 32]. However, the membranes containing graphene oxide-based nanoplatelets had larger pores than the pristine PCL membranes (Figure 2). The cross section of the PCL/rGO membranes was asymmetric and showed that the pore size progressively increased from the top to the bottom of the membrane. Although the PCL/GO and PCL/GO/UV membranes presented a slight reduction in the bulk porosity that was statistically significant (in contrast to the PCL membranes), this parameter presented values between 75 to 80% for all 4 types of membranes (Table 1). Moreover, the pores of the PCL/GO and PCL/GO/UV membranes were actually larger than those of the PCL membranes, which was qualitatively observed in the cross-section SEM images (Figure 2). However, the membrane surface porosity decreased from ~40% to 9% when GO nanoplatelets were introduced into the membrane matrix and to 12% when rGO nanoplatelets were incorporated. The incorporation of 0.1wt% GO and rGO in the PCL solution reduced the viscosity from approximately 4900 cP for the pristine PCL solution to 2900 and 2800 cP for the PCL/GO and PCL/rGO solutions, respectively. This viscosity reduction potentially accelerated the solvent-nonsolvent exchange that occurred during phase inversion and led to the formation of larger internal pore sizes and a less porous surface, characteristics of a faster demixing process [3, 33]. In summary, the high total porosity and qualitative pore sizes of the PCL and PCL-graphene oxide membranes (Figure 2) were indicative of microfiltration membranes, ideal for achieving high nutrient transport properties and low pore blockage during cell infiltration [34].

The FTIR-ATR spectra of the synthesized GO and rGO nanoplatelets are featured in Figure 3(a). The FTIR spectrum of GO showed the representative peaks of the nanomaterial, which included the following bands: i) 3551 cm^{-1} corresponding to the stretching vibration of the hydroxyl groups (-OH), ii) 1630 cm^{-1} was assigned to the skeletal vibrations from unoxidized graphitic domains (C=C), and iii) 1718, 1312, 1152 and 1026 cm^{-1} were ascribed to the stretching vibrations of oxygen corresponding to carboxyl (C=O), carboxyl (C-O), epoxy (C-O) and alkoxy (C-O) groups, respectively [35-37]. The characteristic peaks of the oxygenated groups present in the GO clearly disappeared for the hydrothermally reduced GO (rGO), demonstrating sufficient reduction of the material. Raman spectra of GO and rGO (Figure S4 in the supplementary Material) showed the presence of both the G band corresponding to the primary in-plane vibration mode of graphene (at 1580-1600 cm^{-1}) and the D band attributed to the defects of graphene at 3500 cm^{-1} in both nanomaterials. However, the absorbance of the rGO was approximately half of that of the GO nanomaterial confirming as well the partial reduction of the oxygenated groups observed by FTIR-ATR.

Figure 3(b) shows the FTIR-ATR spectra of the PCL and PCL-graphene oxide membranes. The characteristic PCL ester bond at 1725 cm^{-1} can be clearly observed in all the membranes as well as the characteristic stretching -CH_2- vibrational peaks at 2945 and 2865 cm^{-1}. The peak transmittance at 1725 cm^{-1} for PCL was used to normalize the signal for the PCL-graphene membranes. The PCL/GO and PCL/GO/UV membranes presented the characteristic GO peaks corresponding to the presence of unoxidized graphitic domains (C=C) at approximately 1630 cm^{-1}. The transmittance reduction of the C=C peak intensity and its displacement towards the PCL ester bond wavelength (1725 cm^{-1}) for the PCL/GO/UV membranes indicated the partial reduction

of GO and may indicate possible chemical bonding between the graphene oxide and PCL. In the PCL/rGO membranes, the absence of the characteristic rGO transmittance peaks was expected due to the absence of the characteristic IR transmittance peaks observed for rGO in Figure 3a.

The thermal properties of the PCL and PCL-graphene oxide membranes are presented in Figure 4. In Figure 4(a), the DSC thermograms of the PCL and PCL-graphene oxide membranes can be seen. The temperature of crystallization (T_c) was determined from the first ramp of cooling, and the melting temperature (T_m) was determined from the second heating ramp. The presence of graphene oxide-based nanoplatelets slightly increased both the T_c and T_m values compared to those of the plain PCL membranes (Table 2). The value of T_c for the PCL membrane increased from 31.75°C to 32.45°C for the PCL/rGO membranes and to 33.58°C for the PCL/GO membranes, which corresponded to the nucleating effect caused by the presence of graphene oxide-based nanoplatelets in the polymer matrix. This result is in agreement with the observed increase in the degree of crystallinity, χ_C (%), when graphene oxide-based nanoplatelets were incorporated into the matrix of the PCL membranes (Table 2). The slightly higher T_c of the PCL/GO membranes could have been caused by van der Waals interactions between the PCL and GO [24]. The PCL/GO/UV membranes indicated a reduction in crystallinity in comparison to the PCL/GO membranes (Table 2). Although the irradiation of UV light through PCL membranes has been reported to cause photodegradation of the amorphous phase of the polymer and thus increase the degree of crystallinity [38, 39], the UV phototreatment of PCL/starch blend composites with 5wt% and 20wt% sisal fibres for 6 days reduced the crystallinity between 25% and 60% due to the breakdown of the crystalline phase of the PCL chains [38].

The TGA curves in Figure 4(b) show the thermal stability of the PCL and PCL-

graphene oxide membranes. Incorporating graphene oxide-based nanoplatelets at the concentration tested in the present study (0.1%w/w) minimally altered the basic thermal degradation properties in comparison to the PCL membrane used as a reference. However, a slight increase in the initial temperature of degradation was observed when rGO nanoplatelets were incorporated (Figure 4(b) and Table 2). The weight loss of the PCL/GO membranes observed at approximately 200°C was attributed to traces of NMP solvent that remained in the membrane structure.

Figure 5 and Table 3 show the axial tensile stress-strain curves and characteristic mechanical properties, respectively, of the PCL and PCL-graphene oxide membranes. At the graphene oxide-based nanoplatelet concentration used in this study (0.1 wt%), the elastic modulus and the yield stress of the PCL-graphene oxide membranes did not vary significantly in comparison to the pristine PCL membrane properties but slightly increased for the PCL/GO and PCL/GO/UV membranes and decreased for the PCL/rGO membranes (see Table 3). The presence of graphene oxide-based nanoplatelets in the PCL membranes significantly reduced the mechanical properties at rupture for the PCL/rGO membranes and slightly decreased them for the PCL/GO and PCL/GO/UV membranes in comparison to the plain PCL membranes (Figure 5 and Table 3). Similar behaviour was observed by Sayyar et al. [27] and Wang et al. [28] for PCL-graphene oxide-based composites prepared by mixing and covalent chemical bonding, which was attributed to a restriction of the mobility of the polymer chains due to the presence of the graphene oxide-based nanofillers in the polymer matrix. The improvement in the ultimate elastic modulus from the PCL/GO to the PCL/GO/UV membranes might indicate the presence of certain chemical bonds between PCL and the GO nanoplatelets.

3.2. Membrane flux

In Figure 6(a) and (b) the clean water fluxes (L m^{-2} h^{-1}) at different transmembrane pressures and the hydraulic permeances (L m^{-2} h^{-1} bar^{-1}) are presented, respectively. Compared with the PCL membrane, the PCL/rGO membranes presented significantly higher water fluxes and hydraulic permeances (14437±1860 and 36189±4789 L m^{-2} h^{-1} bar^{-1} for the PCL and PCL/rGO membranes, respectively). This behaviour could be explained by the higher porosity and lower thickness of the limiting layer from the water flux observed in the PCL/rGO membrane explained previously. In contrast, the PCL/GO (4685±1860 L m^{-2} h^{-1} bar^{-1}) and PCL/GO/UV (3507±1067 L m^{-2} h^{-1} bar^{-1}) membranes suffered a significant decrease in their hydraulic permeance, in contrast to the PCL membranes. In this case, the decreased hydraulic permeance was attributed to the slight decrease in the porosity from the PCL to the PCL/GO and PCL/GO/UV membranes. In comparison to previous works that studied microfiltration polymer membranes for tissue engineering bioreactors, the present PCL and PCL-graphene oxide membranes exhibited comparable or higher hydraulic permeances (Table 4). For instance, Bettahalli et al. [40, 41] reported poly(L-lactic)acid (PLLA) hollow fibre membranes with a hydraulic permeance of 2094 L m^{-2} h^{-1} bar^{-1} and commercial polyethersulfone (PES) and polysulfone (PS) hollow fibre membranes with a hydraulic permeance of 5200 $Lm^{-2}h^{-1}bar^{-1}$. However, the hydraulic permeance of the commercial polypropylene (PP) hollow fibre membrane was 3010 L m^{-2} h^{-1} bar^{-1}. Meneghello et al. [34] found that blended poly(lactic-co-glycolic acid)/polyvinyl alcohol (PLGA-PVA) hollow fibre membranes containing at least 5% PVA had a hydraulic permeance of 12000 L m^{-2} h^{-1} bar^{-1}. In contrast, PLGA-PVA membranes containing lower PVA concentrations did not present any water flux. The PCL hollow fibre membranes to be used as small blood vessel scaffolds exhibited hydraulic permeances between 200 and

800 L m^{-2} h^{-1} bar^{-1} depending on the coagulation bath employed (IPA or water) during their fabrication by phase inversion [42].

In Figure 6(b), the total permeance of the model BSA solution for the PCL and PCL-graphene oxide membranes significantly decreased by a factor of 8-17 with respect to the hydraulic permeance. However, the PCL/rGO membranes still exhibited a very high total BSA solution permeance and low BSA rejection (4140 L m^{-2} h^{-1} bar^{-1} and 1.6%, respectively). In contrast to the hydraulic permeance, total cell culture medium-solution permeance reductions between 5 and 10 times were also observed in the commercial microfiltration PES (from ~5500 to 1040 L m^{-2} h^{-1} bar^{-1}), PS (from ~5000 to 660 L m^{-2} h^{-1} bar^{-1}) and PP (from ~3000 to 300 L m^{-2} h^{-1} bar^{-1}) hollow fibre membranes [41] (Table 4). This behaviour was attributed to a fouling effect. Among the possible fouling mechanisms for microfiltration membranes ((1) internal fouling due to pore narrowing, (2) pore blockage due to aggregated proteins and (3) protein deposition on the membrane surface [34, 43]), the most likely fouling mechanism in the present microfiltration PCL and PCL-graphene oxide membranes was considered to be internal fouling due to pore narrowing because of the surface and cross-section morphologies of the membranes (the porosity and qualitative pore size SEM images are shown in Figure 2). Bowen and Gan [44] proposed that this internal fouling phenomena occurred due to internal protein adsorption on the microfiltration membranes, which was in agreement with the high decrease in the total flux that was observed (approximately 82% for the PCL membranes, 95% for the PCL/GO and PCL/GO/UV membranes and 90% for the PCL/rGO membranes) during the present filtration experiments and the low BSA rejection values (between 2 and 20%), as shown in Figure 6b. According to Haggen-Poiseulle equation, the flux reduction of the PCL and PCL-graphene oxide membranes could be caused by a 3-fold reduction of the effective pore size, that still would remain

sufficiently large to allow BSA transport to the permeate side (BSA has approximately a hydrodynamic molecular size of 10 nm at the working pH [45]). Despite the total BSA solution flux reduction observed in the experiments, a theoretical culture medium permeance of 250 L $m^{-2}h^{-1}bar^{-1}$ was previously found to be sufficient for supplying glucose to enable 3-layer cell survival in a bioreactor [41]. Therefore, even the lowest permeability membrane, PCL/GO/UV, with a total permeance of 310 L m^{-2} h^{-1} bar^{-1}, could sustain a multilayered cell culture per unit of the active membrane area.

3.3. Membrane biocompatibility

Figure 7 presents confocal microscopy images at different proliferation time points for the U87 glioblastoma cells on the PCL and PCL-graphene oxide membranes that were used in a preliminary evaluation of their biocompatibility while supporting a culture of neural cells for tissue engineering applications. Although the cell adhesion at day 1 in the PCL and PCL-graphene oxide membranes was similar, the confocal images show that the U87 cells on the PCL membranes formed clusters and were not uniformly distributed on the surface. In contrast, the presence of graphene oxide-based nanoplatelets in the PCL membranes enhanced the cell distribution during cell attachment. Similarly, at days 6 and 14 in the culture, the cells in the PCL membranes were scarce and were not uniformly spread throughout the membrane surface. The introduction of graphene oxide-based nanoplatelets resulted in a higher cell abundance on the membrane surface as well as a sprouted cell morphology in comparison to the PCL membranes. Therefore, the presence of graphene oxide-based nanoplatelets on the polymer matrix enhanced the PCL membrane biocompatibility towards the neural glioblastoma cell line. These results agree with previous works in which scaffolds prepared only with graphene [46] or graphene oxide [47] or by incorporating rGO or GO nanoplatelets into polymer scaffolds [21, 27] exhibited biocompatibility. Therefore,

these results confirm that the PCL-graphene oxide membranes prepared in the present study are potentially useful as scaffolds in bioreactors for neural tissue applications.

4. CONCLUSIONS

In this study, we developed PCL-graphene oxide membranes that possess outstanding transmembrane fluxes for water and BSA protein solutions, which are key features for applications in cell culture bioreactors. The PCL-graphene oxide membranes were fabricated by using phase inversion techniques, mild temperature conditions and nontoxic reductive reagents, in contrast to previously reported methods. The spectroscopic and mechanical results indicated that the PCL/GO/UV membranes could have formed covalent bonds between PCL and the reduced GO particles; however, the thermal DSC observations indicated that van der Waals interactions between PCL and the GO nanoplatelets could have occurred. In general, the experimental results did not provide solid evidence of the formation of nanocomposites in the PCL-graphene oxide membranes, probably due to the low graphene oxide-based nanoplatelets content (0.1%w/w) that was successfully loaded into the PCL matrix. Therefore, the PCL-graphene oxide membranes prepared herein are considered as mixed-matrix membranes. The incorporation of graphene oxide-based nanoplatelets into the polymer matrix did not reinforce the mechanical properties of the PCL membranes. In contrast, the presence of graphene oxide-based nanomaterials might have restricted the polymer chain mobility, reducing the elongation and ultimate strain in comparison to the PCL control membranes. The PCL-graphene oxide membranes were mechanically stable, and the mechanical properties were sufficient to enable their use as scaffolds for cell proliferation in perfusion bioreactors. The PCL-graphene oxide membranes exhibited a highly interconnected porous structure and, as mentioned previously, had outstanding

nutrient transport properties for use in bioreactors in tissue engineering applications. Particularly, the PCL/rGO membranes had higher transport properties than the PCL, PCL/GO and PCL/GO/UV membranes and other biocompatible polymer membranes reported elsewhere. This transport behaviour was attributed to the higher pore size and asymmetric pore distribution observed in the PCL/rGO membrane morphology in comparison to the PCL, PCL/GO and PCL/GO/UV membranes. The nutrient transport properties were characterized by conducting BSA filtration experiments, and the PCL/rGO membranes had lower BSA rejection rates and higher permeances than the rest of the membranes and could support better multilayered cell cultures in the bioreactors.

Finally, the biocompatibility tests demonstrated that the PCL membranes containing graphene oxide-based nanoplatelets presented more uniform glioblastoma cell distributions and better cell morphologies in comparison to the plain PCL membranes. In conclusion, the PCL-graphene oxide membranes prepared herein by using a facile fabrication method and nontoxic reagents presented promising properties and should be studied further for dynamic cell culturing and neural stem cell differentiation.

Acknowledgements

Financial support of the Cantabria Explora call through project JP03.640.69 is gratefully acknowledged. The authors would like to thank Dr. Fidel Madrazo (Advanced Optical Microscopy Services, IDIVAL) for his help with the confocal microscopy experiments. The SEM images and tensile tests were performed in the Laboratorio de la División de Ciencia y Tecnología de los Materiales (LADICIM) of the University of Cantabria (UC) and the DSC results were characterized by the Servicio de Caracterización de Materiales (SERCAMAT, UC).

APPENDIX A. SUPPLEMENTARY MATERIAL

The supplementary material of this article includes a comparison of the PCL/GO membranes produced using 0.1 %w/w and 1%w/w of GO (Figure S1), micro-photographs of the surface of the GO and rGO nanomaterials captured by a confocal microscope (20X) installed in the Raman spectrometer T64000 (Horiba) (Figure S2), the average particle size distributions (Figure S3) of GO and rGO dispersed in NMP analysed using DLS (Zetasizer Nano Series, Malvern) with a standard spherical particle model and the Raman spectra (Raman spectrometer T64000, Horiba) of the GO and rGO nanoplatelets (Figure S4). The excitation wavelength was 514 nm from a Krypton-Argon laser. The spectrometer is also equipped with a Charge Coupled Device (CCD) detector cooled with liquid nitrogen.

REFERENCES

[1] D.F. Stamatialis, B.J. Papenburg, M. Gironés, S. Saiful, S.N.M. Bettahalli, S. Schmitmeier, M. Wessling, Medical applications of membranes: Drug delivery, artificial organs and tissue engineering, J. Membr. Sci. 308 (2008) 1-34.

[2] N. Diban, D. Stamatialis, Polymeric hollow fiber membranes for bioartificial organs and tissue engineering applications, J. Chem. Technol. Biotechnol. 89 (2014) 633-643.

[3] J. Yin, B. Deng, Polymer-matrix nancomposite membranes for water treatment, J. Membr. Sci. 479 (2015) 256–275.

[4] V. Vatanpur, S.S. Madaeni, R. Moradian, S. Zinadini, B. Astinchap, Novel antibifouling nanofiltration polyethersulfone membrane fabricated from embedding TiO2 coated multiwalled carbon nanotubes, Sep. Purif Technol. 90 (2012) 69-82.

[5] S. Zinadini, A.A. Zinatizadeh, M. Rahimi, V. Vatanpour, H. Zangeneh,

Preparation of a novel antifouling mixed matrix PES membrane by embedding graphene oxide nanoplates, J. Membr. Sci. 453 (2014) 292-301.

[6] M.C. Serrano, M.C. Gutiérrez, F. del Monte, Role of polymers in the design of 3D carbon nanotube-based scaffolds for biomedical applications, Prog. Polym. Sci. 39 (2014) 1448–1471.

[7] S. Kumar, S. Raj, E. Kolanthai, A.K. Sood, S. Sampath, K. Chatterjee, Chemical functionalization of graphene to augment stem cell osteogenesis and inhibit biofilm formation on polymer composites for orthopedic applications, ACS Appl. Mater. Interfaces 7 (2015) 3237−3252.

[8] J.-S. Li, Y. Li, X. Liu, J. Zhang, Y. Zhang, Strategy to introduce an hydroxyapatite–keratin nanocomposite into a fibrous membrane for bone tissue engineering, J. Mater. Chem. B 1 (2013) 432-437.

[9] H. Liao, K. Shi, J. Peng, Y. Qu, J. Liao, Z. Qian, Preparation and properties of nano-hydroxyapatite/gelatin/poly(vinyl alcohol) composite membrane, J. Nanosci. Nanotechnol. 15 (2015) 4188-4192.

[10] M. Rai, A. Yadav, A. Gade, Silver nanoparticles as a new generation of antimicrobials, Biotechnol. Adv. 27 (2009) 76-83.

[11] A. Agarwal, T.L. Weis, M.J. Schurr, N.G. Faith, C.J. Czuprynski, F.J. McAnulty, C. J. Murphyd, N.L. Abbotta, Surfaces modified with nanometer-thick silver-impregnated polymeric films that kill bacteria but support growth of mammalian cells, Biomaterials 31 (2010) 680-690.

[12] I. Armentano, M. Dottori, E. Fortunati, S. Mattioli, J.M. Kenny, Biodegradable polymer matrix nanocomposites for tissue engineering: A review, Polym. Degrad. Stab. 95 (2010) 2126-2146.

[13] S.P. Lonkar, Y.S. Deshmukh, A.A. Abdala, Recent advances in chemical modifications of graphene, Nano Res. 8 (2015) 1039–1074.

[14] H.Y. Mao, S. Laurent, W. Chen, O. Akhavan, M. Imani, A.A. Ashkarran, M. Mahmoudi, Graphene: promises, facts, opportunities, and challenges in nanomedicine, Chem. Rev. 113 (2013) 3407−3424.

[15] X. Ding, H. Liu, Y. Fan, Graphene-based materials in regenerative medicine, Adv. Healthcare Mater. 4 (2015) 1451–1468.

[16] Y. Volkov, J. McIntyre, A. Prina-Mello, Graphene toxicity as a double-edged sword of risks and exploitable opportunities: a critical analysis of the most recent trends and developments, 2D Mater. 4 (2017) 02200 (22 pp).

[17] N. Diban, J. Ramos-Vivas, S. Remuzgo-Martinez, I. Ortiz, A. Urtiaga, Poly(ε-caprolactone) films with favourable properties for neural cell growth, Curr. Top. Med. Chem. 14 (2014) 2743-2749.

[18] F. Beckert, C. Friedrich, R. Thomann, R. Mülhaupt, Sulfur-functionalized graphenes as macro-chain-transfer and raft agents for producing graphene polymer brushes and polystyrene nanocomposites, Macromol. 45 (2012) 7083−7090.

[19] B. Chaudhuri, D. Bhadra, L. Moroni, K. Pramanik, Myoblast differentiation of human mesenchymal stem cells on graphene oxide and electrospun graphene oxide-polymer composite fibrous meshes: importance of graphene oxide conductivity and dielectric constant on their biocompatibility, Biofabrication 7 (2015) 015009 (13 pp).

[20] J. Song, H. Gao, G. Zhu, X. Cao, Y. Wang, The preparation and characterization of polycaprolactone/graphene oxide biocomposite nanofiber scaffolds and their application for directing cell behaviors, Carbon 95 (2015) 1039-1050.

[21] C. Wan, B. Chen, Poly(ε-caprolactone)/graphene oxide biocomposites: mechanical properties and bioactivity, Biomed. Mater. 6 (2011) 055010 (8pp)

[22] A. Patel, Y. Xue, S. Mukundan, L.C. Rohan, V. Sant, D.B. Stolz, S. Sant, Cell-instructive graphene-containing nanocomposites induce multinucleated myotube formation, Ann. Biomed. Eng. 44 (2016) 2036-2048.

[23] B. Holmes, X. Fang, A. Zarate, M. Keidar, L.G. Zhang, Enhanced human bone marrow mesenchymal stem cell chondrogenic differentiation in electrospun constructs with carbon nanomaterials, Carbon 97 (2016) 1 –13.

[24] S. Ramzani, M. Karimi, Aligned poly(ε-caprolactone)/graphene oxide and reduced graphene oxide nanocomposite nanofibers: Morphological, mechanical and structural properties, Mater. Sci. Eng. C 56 (2015) 325–334.

[25] H. Niu, T. Lin, Fiber generators in needleless electrospinning, J. Nanomater. 2012 (2012) 725950 (13 pp).

[26] S.-L. Liu, Y.-Y. Huang, H.-D. Zhang, B. Sun, J.-C. Zhang, Y.-Z. Long Needleless electrospinning for large scale production of ultrathin polymer fibres, Mater. Res. Innov. 18:sup4 (2014), S4-833-S4-837

[27] S. Sayyar, E. Murray, B.C. Thompson, S. Gambhir, G.G. Wallace, Covalently linked biocompatible graphene/polycaprolactone composites for tissue engineering, Carbon 52 (2013) 296-304;

[28] G. Wang, Z. Wei, L. Sang, G. Chen, W. Zhang, X. Dong, M. Qi, Morphology, crystallization and mechanical properties of poly(ε-caprolactone)/graphene oxide nanocomposites, Chinese J. Polym. Sci. 31 (2013) 1148-1160.

[29] W.S. Hummer, R.E. Offeman, Preparation of graphitic oxide. J. Am. Chem. Soc. 89 (1958) 1339-1339.

[30] P. Ribao, M.J. Rivero, I. Ortiz, TiO_2 structures doped with noble metals and/or

graphene oxide to improve the photocatalytic degradation of dichloroacetic acid; Environ. Sci. Pollut. Res. 24 (2017) 12628-12637.

[31] Sigma Aldrich products catalog. http://www.sigmaaldrich.com/catalog/product/aldrich/440744?lang=es&region=ES (accessed 10.09.2016).

[32] N. Diban, D.F. Stamatialis, Functional polymer scaffolds for blood vessel tissue engineering, Macromol. Symp. 309-310 (2011) 93-98.

[33] M. Mulder, Preparation of synthetic membranes, in: Basic principles of membrane technology, Kluwer, Dordrecht, 1996, pp 54-109.

[34] G. Meneghello, D.J. Parker, B.J. Ainsworth, S.P. Perera, J.B. Chaudhuri, M.J. Ellis, P.A. De Bank, Fabrication and characterization of poly(lactic-co-glycolic acid)/polyvinyl alcohol blended hollow fibre membranes for tissue engineering applications, J. Membr. Sci. 344 (2009) 55-61.

[35] D. Liang, C. Cui H. Hu, Y. Wang, S. Xu, B. Ying, P. Li, B. Lu, H. Shen, One-step hydrothermal synthesis of anatase TiO_2/reduced graphene oxide nanocomposites with ehhanced photocatalytic activity, J. Alloys Compd. 582 (2014) 236-240.

[36] Y.H. Ding, P. Zhang, Q. Zhuo, H.M. Ren, Z.M. Yang, Y. Jiang, A green approach to the synthesis of reduced graphene oxide nanosheets under UV irradiation, Nanotechnol. 22 (2011) 215601 (5pp).

[37] B.D. Mistry, A handbook of spectroscopic data: Chemistry (UV, IR, PMR, CNMR and mass spectroscopy), Oxford Book Company, New Delhi, 2009.

[38] A. Campos, J.M. Marconcini, S.M. Martins-Franchetti, L.H.C. Mattoso, The influence of UV-C irradiation on the properties of thermoplastic starch and polycaprolactone biocomposite with sisal bleached fibers, Polym. Degrad. Stab. 97 (2012) 1948-1955.

[39] C.-C. Yeh, C.-N. Chen, Y.-T. Li, C.-W. Chang, M.-Y. Cheng, H.-I. Chang, The effect of polymer molecular weight and UV radiation on physical properties and bioactivities of PCL films, Cell. Polym. 30 (2011) 261-276.

[40] N.M.S. Bettahalli, H. Steg, M. Wessling, D. Stamatialis, Development of poly(l-lactic acid) hollow fiber membranes for artificial vasculature in tissue engineering scaffolds, J. Membr. Sci. 371 (2011)117-126.

[41] N.M.S. Bettahalli, J. Vicente, L. Moroni, G.A. Higuera, C.A. van Blitterswijk, M. Wessling, D.F. Stamatialis, Integration of hollow fiber membranes improves nutrient supply in three-dimensional tissue constructs, Acta Biomater. 7 (2011) 3312-3324.

[42] N. Diban, S. Haimi, L. Bolhuis-Versteeg, S. Teixeira, S. Miettinen, A. Poot, D. Grijpma, D. Stamatialis, Development and characterization of poly(ε-caprolactone) hollow fiber membranes for vascular tissue engineering, J. Membr. Sci. 438 (2013) 29-37.

[43] A. Persson, A.-S. Jönsson, G. Zacchi, Transmission of BSA during cross-flow microfiltration: influence of pH and salt concentration, J. Membr. Sci. 223 (2003) 11–21.

[44] W.R. Bowen, Q. Gan, Properties of microfiltration membranes: flux loss during constant pressure permeation of bovine serum albumin, Biotechnol. Bioeng. 38 (1991) 688– 696.

[45] V.Valiño, M.F. San Román, R. Ibáñez, J.M. Benito, I. Escudero, I. Ortiz, Accurate determination of key surface properties that determine the efficient separation of bovine milk BSA and LF proteins, Sep. Purif. Technol. 135 (2014) 145-157.

[46] N. Li, Q. Zhang, S. Gao, Q. Song, R. Huang, L. Wang, L. Liu, J. Dai, M. Tang, G. Cheng, Three-dimensional graphene foam as a biocompatible and conductive scaffold for neural stem cells, Sci. Rep. 3 (2013) 1604 (6pp).

[47] M.C. Serrano, J. Patiño, C. Garcıa-Rama, M. L. Ferrer, J. L. G. Fierro, A. Tamayo, J. E. Collazos-Castro, F. del Monte, M. C. Gutierrez, 3D free-standing porous scaffolds made of graphene oxide as substrates for neural cell growth, J. Mater. Chem. B, 2 (2014) 5698-5706.

Figure captions

Figure 1. Cross-flow filtration setup.

Figure 2. Cross-section and surface SEM images of the PCL and PCL-graphene membranes. The scale bars represent 10 µm.

Figure 3. FTIR-ATR spectra of the GO and rGO nanomaterials (a) and of the PCL and PCL-graphene membranes (b).

Figure 4. DSC thermograms (a) and TGA profiles (b) of the PCL and PCL-graphene membranes. The inset in (a) shows a magnification of the melting temperature measured during the second heating ramp.

Figure 5. Tensile stress-strain curves of the PCL and PCL-graphene membranes.

Figure 6. Clean water flux at different transmembrane pressures (a) and comparison of the hydraulic and total model BSA solution permeances and BSA rejections (b) of the PCL and PCL-graphene membranes. The statistical significance (§) with $p<0.05$ was calculated using one-way ANOVA considering PCL as the reference.

Figure 7. Confocal microscopy images of the static cell culture of the U87 cells on the PCL and PCL-graphene membranes at days 1, 6 and 14, indicating the

biocompatibility of the membrane substrates. The red colour highlights the cell mitochondria. The scale bar represents 100 µm.

Table 1. Comparison between the morphological parameters of the PCL and PCL-graphene membranes. The statistical significance (§) with $p<0.05$ was calculated using one-way ANOVA considering PCL as the reference.

Membrane	Thickness, δ (µm)	Bulk Porosity, ε (%)	Surface Porosity, ε_s (%)
PCL	91±5	81±1	40±4
PCL/GO	85±6	76±1(§)	9±1(§)
PCL/GO/UV	83±1	77±1(§)	22±2
PCL/rGO	97±8	80±1	13±2(§)

Table 2. Calorimetric and thermal degradation data derived from the cooling and second heating ramp of the DSC and TGA curves of the PCL and PCL-graphene membranes.

Membrane	PCL	PCL/GO	PCL/GO/UV	PCL/rGO
T_c (°C)	31.75	33.58	32.35	32.45
ΔH_c (J/g)	-70.72	-62.93	-56.37	-59.89
T_m (°C)	55.36	55.60	55.59	55.73
ΔH_m (J/g)	48.88	61.21	48.90	57.06
χ_C (%)	35.04	44.17	35.29	41.18
T_{onset} (°C)	272±9	291±11	290±1	319±4
T_{max} (°C)	409±1	411±1	405±5	411±1

Table 3. Comparison between the mechanical parameters of the PCL and PCL-graphene membranes derived from the tensile stress-strain curves. The statistical significance (§) with $p<0.05$ was calculated using one-way ANOVA considering PCL as the reference.

Membrane	PCL	PCL/GO	PCL/GO/UV	PCL/rGO
Young's modulus (MPa)	23.9±1.9	27.2±2.1	24.0±3.4	16.7±1.5
Yield point (MPa)	2.9±0.2	2.5±0.5	2.9±0.2	1.8±0.1
Ultimate tensile strength (MPa)	3.8±0.2	3.7±0.6	4.4±0.2	2.5±0.2(§)
Ultimate strain (%)	100.5±1.5	69.1±6.5(§)	93.5±18.5	51.1±1.7(§)

Table 4. Comparison of the hydraulic and culture/BSA permeances of the present PCL and PCL-graphene oxide membranes with other polymer membranes reported in the literature.

Membrane material	Hydraulic permeance ($L\ m^{-2}\ bar^{-1}\ h^{-1}$)	BSA/Culture medium permeance ($L\ m^{-2}\ bar^{-1}\ h^{-1}$)	Reference
PCL	14437±1860	840±450	Present work
PCL/GO	4685±1860	591±219	Present work
PCL/GO/UV	3507±1067	310±23	Present work
PCL/rGO	36189±4789	4140±89	Present work
PLGA-PVA	12000	-	Meneghello et al [34]
PLLA	2094	-	Bettahalli et al [40]
PES	5200	1040	Bettahalli et al [41]
PS	5200	660	Bettahalli et al [41]
PP	3010	300	Bettahalli et al [41]
PCL	800	-	Diban et al [42]

Highlights

- Novel composite membranes for cell culture perfusion bioreactors were prepared
- Poly(ε-caprolactone) was blended with graphene oxide or reduced graphene oxide
- Phase inversion using non-toxic reductive agents and mild conditions was applied
- The membranes showed exceptionally high water and bovine serum albumin fluxes
- 0.1% w/w of graphene in the base membrane improved the neural cell biocompatibility

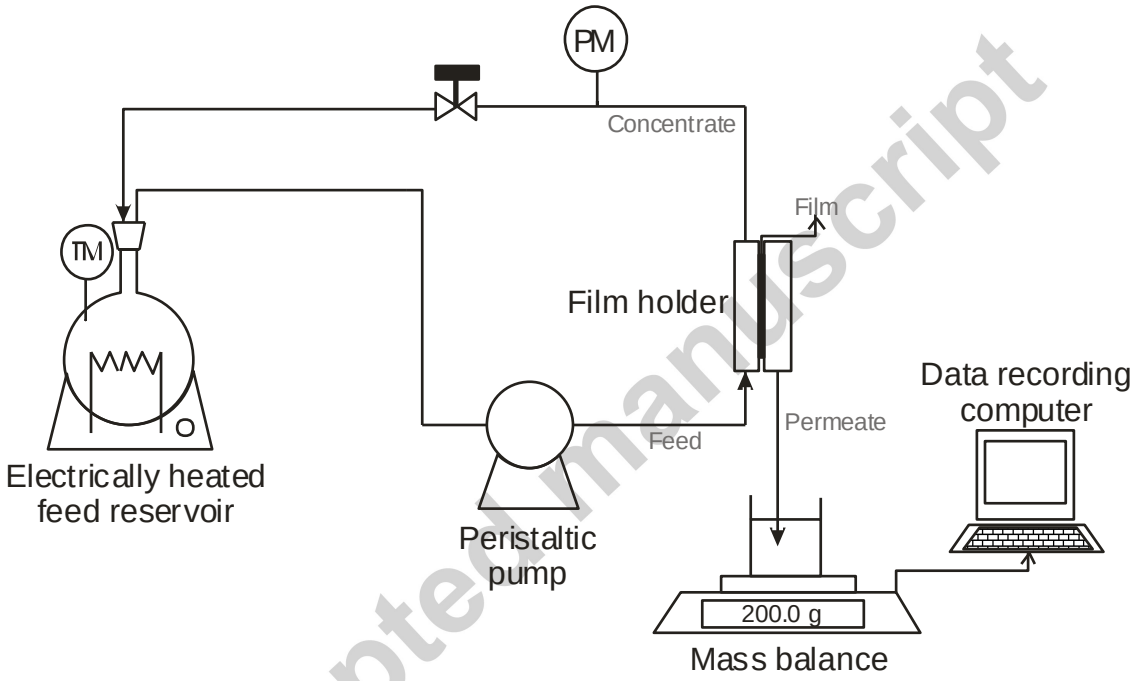

Figure 1.

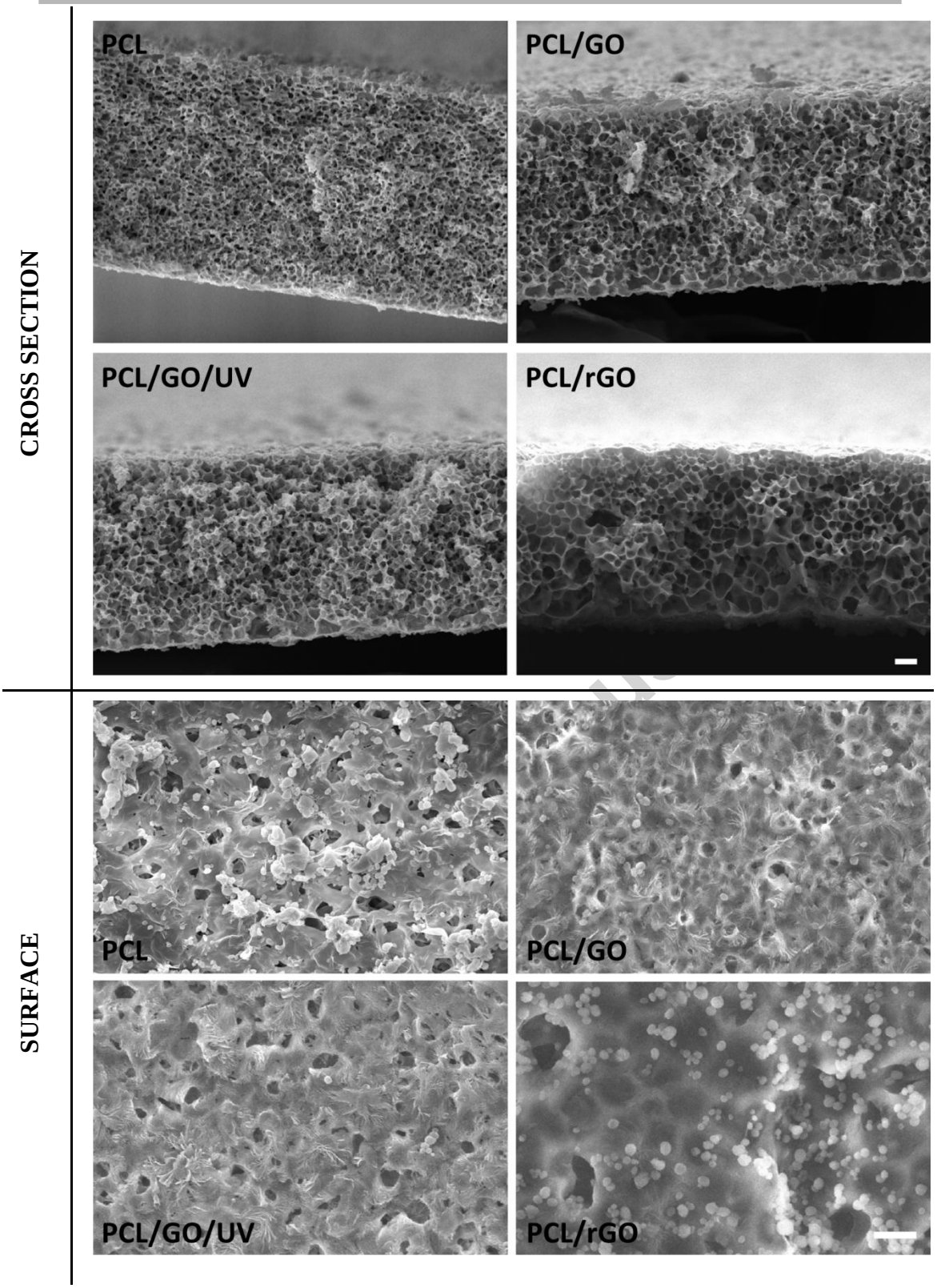

Figure 2.

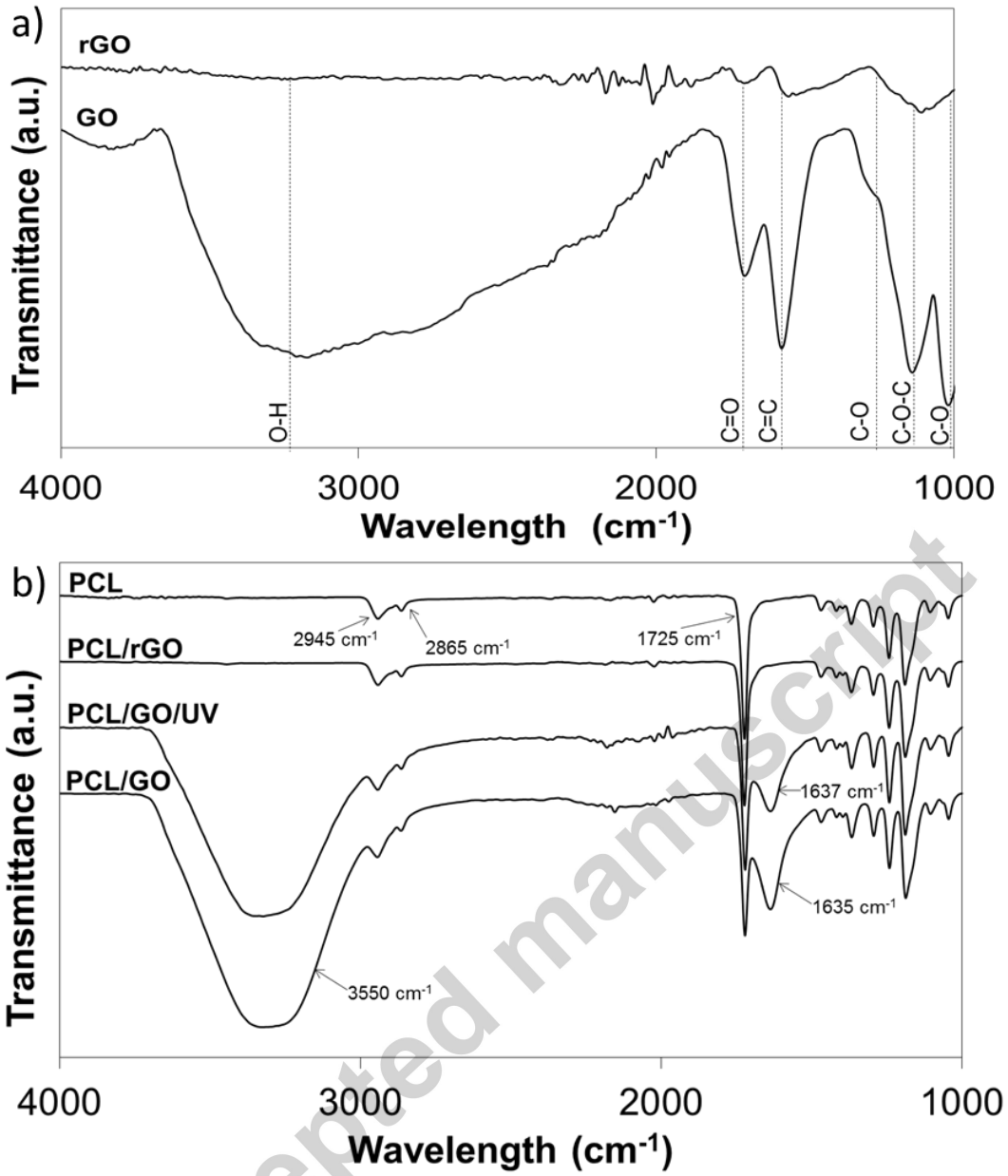

Figure 3.

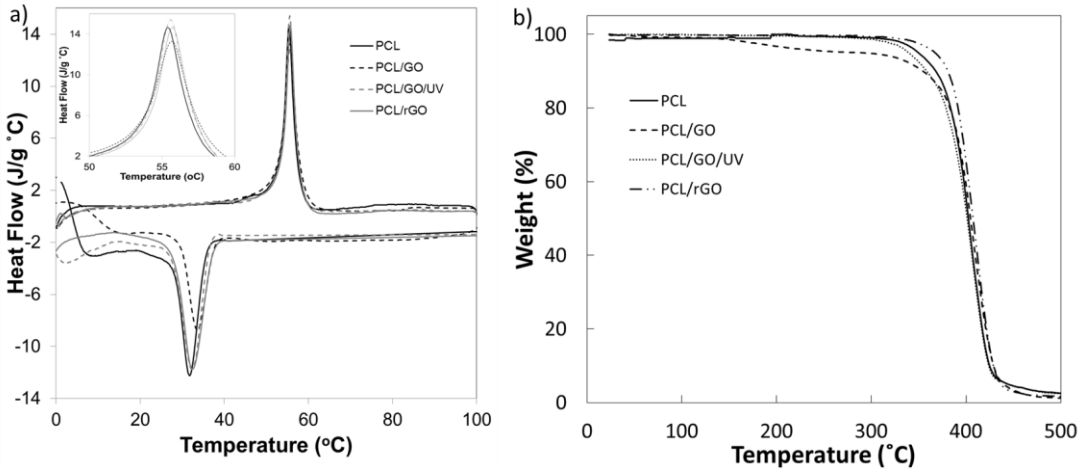

Figure 4.

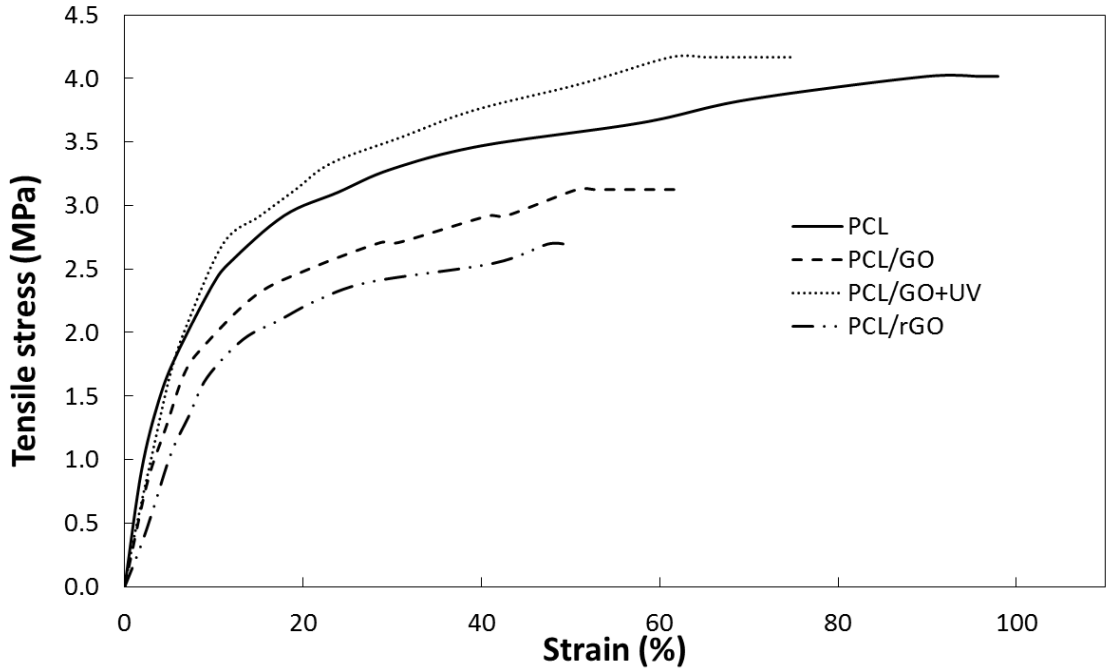

Figure 5.

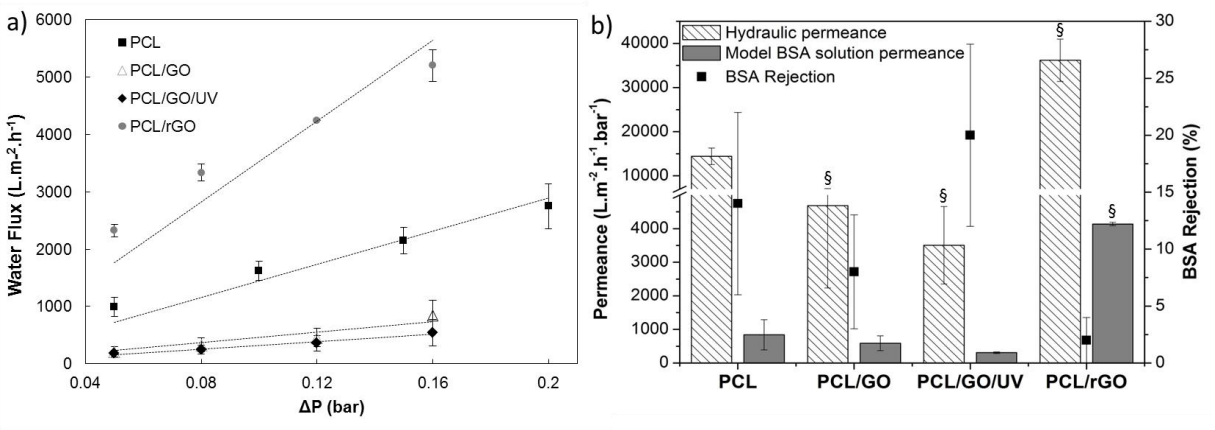

Figure 6.

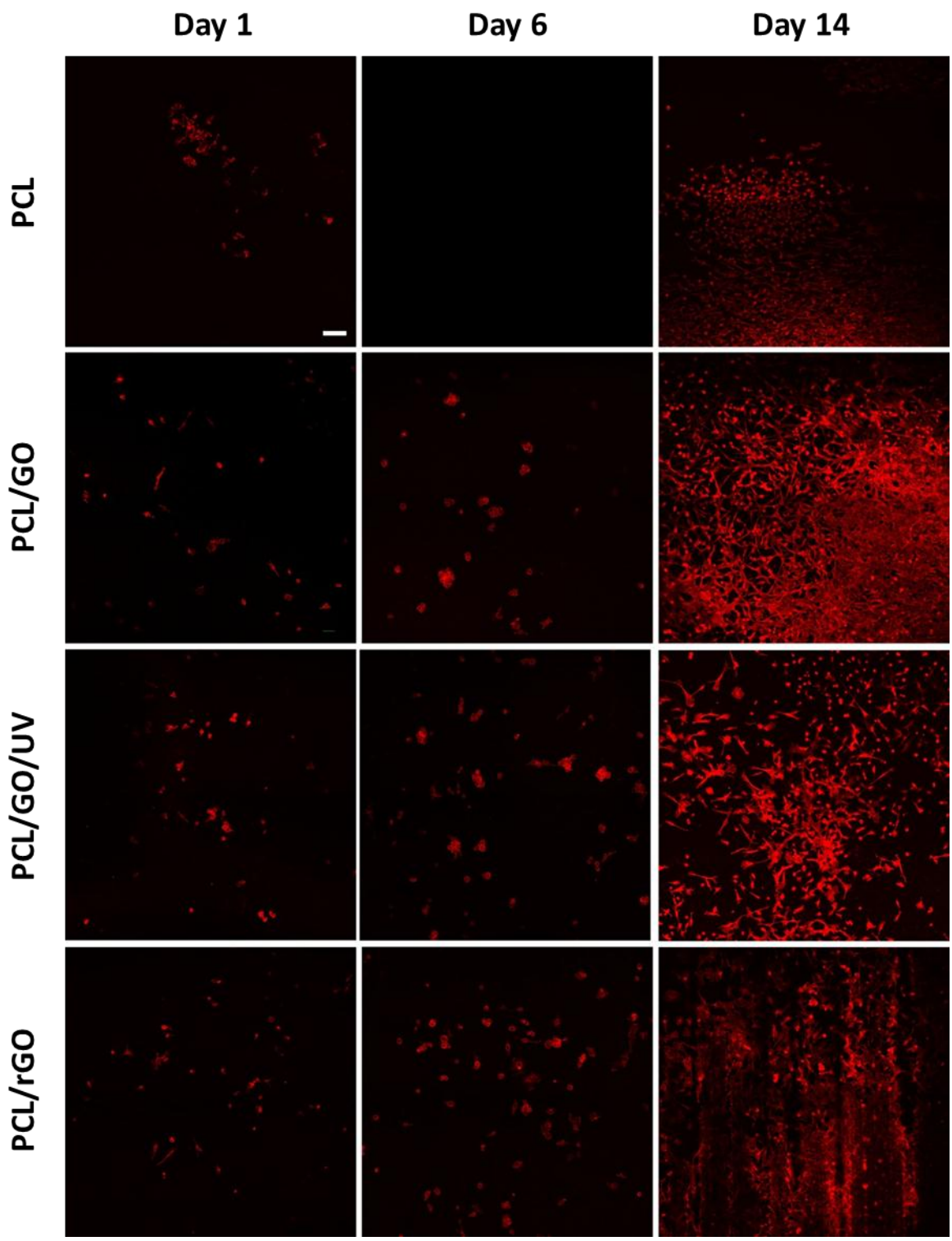

Figure 7.